A fully automated human knee 3D MRI bone segmentation using the ray casting technique

Pierre Dodin, Johanne Martel-Pelletier, Jean-Pierre Pelletier & François Abram

Springer

Springer

ORIGINAL ARTICLE

A fully automated human knee 3D MRI bone segmentation using the ray casting technique

Pierre Dodin · Johanne Martel-Pelletier ·
Jean-Pierre Pelletier · François Abram

Abstract This study aimed at developing a fully automated bone segmentation method for the human knee (femur and tibia) from magnetic resonance (MR) images. MR imaging was acquired on a whole body 1.5T scanner with a gradient echo fat suppressed sequence using an extremity coil. The method was based on the Ray Casting technique which relies on the decomposition of the MR images into multiple surface layers to localize the boundaries of the bones and several partial segmentation objects being automatically merged to obtain the final complete segmentation of the bones. Validation analyses were performed on 161 MR images from knee osteoarthritis patients, comparing the developed fully automated to a validated semi-automated segmentation method, using the average surface distance (ASD), volume correlation coefficient, and Dice similarity coefficient (DSC). For both femur and tibia, respectively, data showed excellent bone surface ASD (0.50 ± 0.12 mm; 0.37 ± 0.09 mm), average oriented distance between bone surfaces within the cartilage domain (0.02 ± 0.07 mm; -0.05 ± 0.10 mm), and bone volume DSC (0.94 ± 0.05; 0.92 ± 0.07). This newly developed fully automated bone segmentation method will enable large scale studies to be conducted within shorter time durations, as well as increase stability in the reading of pathological bone.

P. Dodin · F. Abram
ArthroVision, 1871 Sherbrooke Street East, Montreal,
QC H2K 1B6, Canada

J. Martel-Pelletier (✉) · J.-P. Pelletier
Osteoarthritis Research Unit, University of Montreal Hospital
Research Centre (CRCHUM), Notre-Dame Hospital,
1560 Sherbrooke Street East, Montreal, QC H2L 4M1, Canada
e-mail: jm@martelpelletier.ca

1 Introduction

Magnetic resonance imaging (MRI)-based semi-quantitative and quantitative assessments are increasingly used for evaluation of the efficacy of disease modifying osteoarthritis drugs on knee osteoarthritis patients. As of now, several MRI markers demonstrate strong associations to osteoarthritis, either as predictive markers or markers of disease severity; these include cartilage volume, osteophytes, bone remodelling, bone marrow lesions, meniscal lesions, and synovitis [1, 3, 5, 21, 26, 28]. The majority of these rely on the precise localization of the bone surfaces. Thus, a fully automated precise segmentation of knee bones in MR images is an important step for the automatic evaluation of knee structural changes over time as well as of a drug's effect on the joint.

Particular characteristics of MR images of the joint, including image texture, pigmentation of tissues, contrast between the same tissue from one patient to another, contrast between the slices and within the same image, artifacts, sharpness of contour profile, and position and orientation of the imaged joint, have led to different types of solutions. With regard to the segmentation of knee bones, three types of solutions have been introduced in an attempt to address the abovementioned difficulties. Authors first reported techniques using basic signal analysis, e.g., directional edge filters [31], mathematical morphology [4], gray-level classification [6], histogram analysis [19], and watershed with markers [14], or other techniques including the hybrid signal and model, e.g., texture level-set [23] and model fitting [7, 10, 16, 17]. However, all of these solutions require specific tuning depending on the variable image

quality or the signal deterioration due to disease. This tuning relies on initial manual intervention, additional signal information, or interactive tuning, which makes the autonomous use of these methods difficult in the context of a large scale process in addition to significantly decreasing the stability of bone segmentation, thus the success rate.

For example, the basic signal analysis using directional edge filters to detect the femur contours, as well as other segmentation initialization techniques [4, 6, 19, 31], needs refinement to meet the required precision level. The watershed with markers [14] does not allow easy control of segmentation leakage or object tessellation. Both result in a lack of stability and excessive sensitivity to noise as reported by Hamarneh et al. [15]. For their part, techniques using hybrid signals and models [23] implicate difficulties in controlling the impact of parameters on the outcome; too much weight is placed on the model to prevent segmentation drift at the expense of the signal and of the stability of the result. In addition, model fitting [11, 16] does not implement disease characteristics, but rather is over-constrained by geometric prior. Other techniques use phase information [8], which is not available from MR exams in clinical study, or additional MR information specific to bone segmentation [2], which would increase the exam acquisition time. Although the latter [2] segmentation approach most closely resembles the method reported here, it would require an additional non fat saturated MR sequence for fully automated bone segmentation.

Our developed fully automated method relying on easy-to-gather input information from a single MRI acquisition provides stable results, and is robust to the variable image quality. This is reflected by the validation analyses using quality metrics techniques such as for the bone surface, the average surface distance (ASD) for the bone volume, the Dice similarity coefficient (DSC), and the average oriented distance between bone surfaces within the cartilage domain which all demonstrated excellent data in terms of stability and accuracy. Hence, the reported method leads to a fully automated stable and reproducible knee bone reading and allows the assessment of changes in pathological bone.

2 Method

2.1 Fully automated bone segmentation

2.1.1 Notations

The input information is a gray-level 3D MR image I in which the gray level i at position (x, y, z) is such that $i = I(x, y, z)$. For notation simplification, the slices of an MR image volume will be noted as the 2D images

$$I_{x=h} \equiv \{I(x,y,z)/x=h\} \quad I_{y=c} \equiv \{I(x,y,z)/y=c\}$$
$$I_{z=t} \equiv \{I(x,y,z)/z=t\} \tag{1}$$

These 2D images, defined as 3D image restrictions, consist of gray level values.

In the same way, we define the image domain Ω as the set of all positions (x, y, z) and the slices as the restriction for position sets: $\Omega_{x=h} = \{(y,z)/I_{x=h} > 0\}$, idem for $\Omega_{y=c}$, $\Omega_{z=t}$. These 2D image domains are defined, respectively, as axial, coronal, and sagittal slices.

2.1.2 Localization of the solution

In addition to the MR image, the Ray Casting technique requires an approximate localization of both the femur and the tibia. This is obtained by evaluating an approximation of the femur's interior noted IFemur $\subseteq \Omega$ and an approximation of the tibia's interior, ITibia $\subseteq \Omega$. Because the background and the bone are of the same color and texture, the localization of the bones first relies on an analysis of the leg tissues which is the biggest sub-part of the image made of bright tissues. Then, leg tissue layers are successively filtered until the inner bone is found, providing an approximation of each bone as a 3D object. The overall process is detailed in the Appendix.

2.1.3 Definition of observers

From the approximate bone objects, a series of 3D positions inside each object, named "observers," is necessary as an input data for the Ray Casting technique. The localization procedure for the observers is explained only for the femur, since it is the same for the tibia. A height h is determined on the axial axis at the location where $IFemur_{x=h}$ becomes a single connected component, as shown in Fig. 1. At this height h, we assume the set $IFemur_{z=t,x=h}(y) \equiv IFemur_{x=h}/z=t$ for each $z = t$ to also be a single connected component set. This set provides the most internal point c in the femur by:

$$c(z) = \frac{1}{2}\max\left(y \in IFemur_{z=t,x=h}\right) +$$
$$\frac{1}{2}\min\left(y \in IFemur_{z=t,x=h}\right) \quad \text{for } z = t \tag{2}$$

Note that it can happen that $IFemur_{z=t,x=h}$ is in more than one component. In such a case $IFemur_{z=t,x=h}$ is replaced by its largest component since it is a robust way to maintain the path inside the femur.

This procedure allows the set of observers to be defined as: $o(z) = (h, c(z), z)$
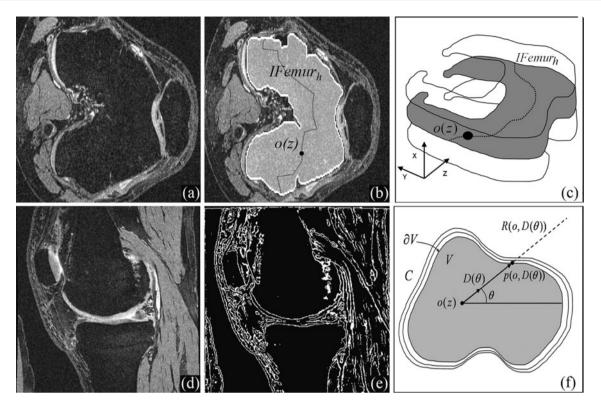
Fig. 1 a Representative axial MR image reconstructed from sagittal acquisition; **b** IFemur$_h$ (*white* contour) is used to locate the observers $o(z)$ in the bone along each slice describing a path (*dotted black line*); **c** 3D schematic representation showing the observer path in the first distal axial slice where IFemur$_h$ is in a single component; **d** representative sagittal MR image; **e** the Laplacian contour set C which is further used by the Ray Casting technique to precisely locate the solution; and **f** the projection of the observer position on the object frontier at all angles θ. $o(z)$ is the observer position in the current image, $R(o, D(\theta))$ is the ray launched from the observer in direction $D(\theta)$, and $p(o, D(\theta))$ is the location of the first intersected contour of set C. Sampling $[0, 2\pi]$ with θ enables identification of surface ∂V delimiting volume V

2.1.4 Construction of the set C of discretized surfaces for Ray Casting purposes

As a second input, the Ray Casting technique requires the set C of all candidate interfaces, i.e., the interfaces between the different tissues that can be extracted from the MR image as illustrated by Fig. 1d.

The Laplacian operator [32] gives a binary map Δ of the presence or absence of all tissue interfaces at each position (x, y, z) in the MR images. Hence a set C, of all interface positions (x, y, z) present in Δ, is computed. This set C is illustrated in Fig. 1e as a precise frontier candidate of Laplacian contours. The final solution consists of a selection of candidates among C using the Ray Casting technique as illustrated in Fig. 1f.

The femur or the tibia bones are represented as an object V with object frontier ∂V. This frontier is contained in the set of all possible frontiers, the set C. For Ray Casting purposes, a ray $R(o, D)$ is defined as the half-line starting from o, in direction D, as shown in Fig. 1f.

Hence the projection into the subset of all possible frontiers of the observer position o in direction D is obtained as an intersection. This is the first intersection of the ray $R(o, D)$ with C. This projection is an element of ∂V, and is written as $p(o, D)$. This is geometrically illustrated in Fig. 1f.

2.1.5 Construction of the sagittal Ray Casting surface using ray patterns

To select the frontier ∂V samples attainable by rays from o, ray patterns were used. The first example of ray pattern is the circular parameterization parallel to each 2D Cartesian plane (x, y). If θ is the angle defined on the unit circle of the (x, y) plane, and M the sample set size of selected angles (e.g., $M = 315$), as shown in Fig. 2a, the ray pattern is obtained as:

$$\text{Circular}(o(z)) = \{ p(o(z), D(\theta_1)) , \ldots, p(o(z), D(\theta_M)) \}$$

For a sagittal observer $o(z)$, an example of Circular $(o(z))$ samples is shown in Fig. 2b. The result is a sequence of points describing a contour in the image. Using multiple observers $Z = \{o(z_1), \ldots, o(z_N)\}$, the circular patterns are combined to obtain a sagittal cylindrical pattern (Fig. 2c), using M the sample set of possible observers as:
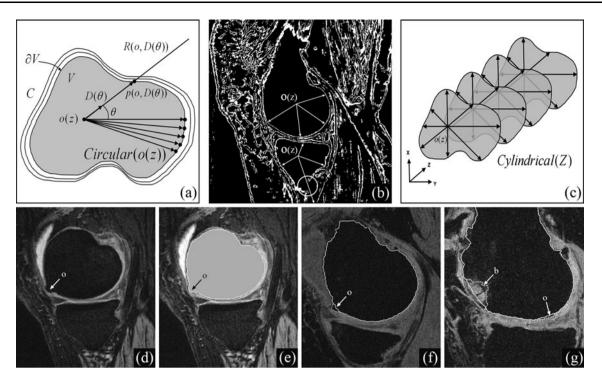
Fig. 2 **a** Description of Ray Casting, **b** a sagittal slice of Δ shows circular($o(z)$) samples, and **c** the cylindrical set. Of note, an open interface (**b** *white circle*) may provoke samples to escape at infinity. **d**, **e** A case of bone segmentation where the osteophyte (*white arrow o* in **d**) is completely captured by the segmentation strategy (*black arrow o* (**e**)). **f**, **g** two examples of the surface of bone (*dotted line*) after controlled surface filtering of the Ray Casting detected bone surface (*solid line*). **f** Complete segmentation of the femur which contains an osteophyte (*arrow o*). **g** Filtering of a major bone marrow lesion (*arrow b*) as well as a small osteophyte (*arrow o*). Osteophyte (*o*) and bone marrow lesion (*b*)

$$\text{Cylindrical}(Z) = \{\text{Circular}(o(z_1)), \ldots, \text{Circular}(o(z_N))\}$$

Since Cylindrical (Z) is a bivariate discrete set by definition, it leads naturally to a discrete surface. But using bicubic spline smoothing interpolation, a continuous closed spline surface noted $\overline{\text{Cylindrical}}(Z)$ was obtained, whose interpolation nodes were given by Cylindrical (Z). Finally, the sagittal Ray Casting surface was the surface $\overline{\text{Cylindrical}}(Z)$

Of note, it can happen that set C of discretized surfaces is not closed while some holes can occur in low contrast zones (e.g., Fig. 2b in the tibia). In such a case, the surface sample "escapes" at infinity. However, this situation, which occurs only in extra articular areas, affects the surface generation only very locally, preserving the accuracy of the solution. This contrasts with watershed or region-growing based methods [2, 14] in which the entire solution is affected.

The Ray Casting technique allows the segmentation of local bone growth as shown in Fig. 2d, e. Such bone protrusion which can appear on as few as one or two slices may not be captured by model-based segmentation [10, 16] in which this shape would be taken as an error.

2.1.6 Controlled surface filtering: first step for solving occultation difficulties

Signal quality or bone geometry may preclude the segmentation process from achieving the proper detection of the bone interface. A smoothing strategy is first applied to remove imperfections that are due to the presence of edges inside the bone (acquisition artifacts or bone lesions) or missing boundaries.

For this aim, we chose the median filter to preserve edges of objects that are wider than half of the filtering window size, as other filtering approaches, e.g., average or Gaussian filter, would systematically fade all edges. Then, an operation of median filtering followed by a restoration is applied iteratively to the bone surface in the cylindrical coordinate system. The purpose of the median filter is to remove imperfections from the surface while the restoration preserves the measured surface where the filtering action is smaller than a threshold. The first iteration allows the threshold to be computed as 2*sigma of the evolution between measured and filtered data but no less than 1.3 mm. At each iteration, the restored surface is marked and is excluded from further processing. In addition, the

size of the filtering window increases from 1 by 10 mm up to 11 by 40 mm, the maximum number of iteration being five. The parameters used allow the filtering of imperfections up to 20 mm in the sagittal plane by 5.5 mm in the transversal direction. Most infinity sample escapes are then managed by this approach. Figure 2f illustrates the effect of the controlled surface filtering process on the bone contour in one sagittal MR image: the process enables the filtering of osteophytes and bone marrow lesions, obtaining the final bone surface of the sagittal analysis.

2.1.7 Solving occultation by merging sagittal and axial segmented bone surfaces

To handle specific morphologies, the presence of bone lesions or extreme positioning of the knee during acquisition that may preclude the capture of the entire bone surface, we implemented an additional Ray-casting segmentation process in the axial plane. This additional segmentation was chosen to be performed in the axial rather than in the coronal reconstructed images as this orientation best addresses the issue of a missing surface. Therefore, a technique referred to as the combination operator $\oplus$ was developed to merge several segmented objects into a single one as illustrated by the 2D example in Fig. 3.

The initial sagittal segmentation result is used as a new description of the femur's interior. This time, two sagittal slices are chosen at the central position of each condyle. For both condyles, a family of observers parameterized in coordinate x is set in the posterior of the condyle assuming the orientation of the acquisition. Once these new families
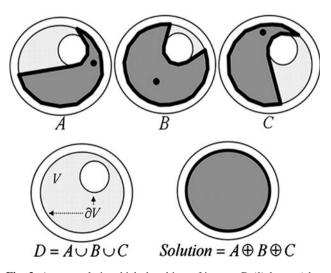

Fig. 3 An example in which the object of interest D (*light gray*) has an outer and an inner interface; D is the union of the Ray Casting solution A, B and C found using different observers initialized inside D. The solution using the combination operator selects the outermost contour of the object

of observers are automatically defined, an axial segmentation is processed. The step by step procedure is formulated as follows. First, the interior ISFemur of SFemur $\equiv \overline{\text{Cylindrical}}(Z)$ is constructed by performing a detection by Ray Casting algorithm. Then, starting from more precise information on the interior than the approximation IFemur, the two families of observers are computed, in the mean slice of left condyle l and in the mean slice of right condyle r, respectively, located in the two sagittal slices ISFemur$_{z=l}$ and ISFemur$_{z=r}$.

ISFemur$_{z=l}$ is a bounded surface in coordinate x and y in one connected component (Fig. 4a) and ISFemur$_{x=h,z=l} =$ ISFemur$_{z=l}/x = h$ (Fig. 4b) is expected to be a single component. If not, it is replaced by its largest component. The observer position is set near the posterior boundary of the component by weighting the maximum part of the segment by a parameter α close to 1:

$$
\begin{aligned}
c_l(x) &= \alpha \max\left(y \in \text{ISFemur}_{x=h,z=l}\right) + (1-\alpha)\min \\
&\quad \left(y \in \text{ISFemur}_{x=h,z=l}\right) \text{ for } x = h \\
c_r(x) &= \alpha \max\left(y \in \text{ISFemur}_{x=h,z=r}\right) + (1-\alpha)\min \\
&\quad \left(y \in \text{ISFemur}_{x=h,z=r}\right) \text{ for } x = h
\end{aligned}
\tag{3}
$$

This leads to the set of observers parameterized in x as

$$
o_l(x) = (x, c_l(x), l) \quad o_r(x) = (x, c_r(x), r).
\tag{4}
$$

and to two families of observers describing a path.

The new axial Ray Casting surfaces are then obtained by using a circular parameterization parallel to each 2D Cartesian plane (y, z) and a set of observers defined along the axial dimension (Fig. 4c). This set is given by $X_r = \{o_r(x_1), \ldots, o_r(x_N)\}$ and $X_l = \{o_l(x_1), \ldots, o_l(x_N)\}$ (Fig. 4d), leading to the axial Ray Casting surfaces $\overline{\text{Cylindrical}}(X_r)$ and $\overline{\text{Cylindrical}}(X_l)$. By convention, if the observer is parameterized in a dimension, the angles of the rays are within the two others, e.g., for X_r and X_l the angle is defined on the unit circle of the (y, z) plane. The final global surface solution combining all the three surfaces is then:

$$
\begin{aligned}
\text{Femur} &= \overline{\text{Cylindrical}}(Z) \oplus \overline{\text{Cylindrical}}(X_r) \\
&\quad \oplus \overline{\text{Cylindrical}}(X_l)
\end{aligned}
\tag{5}
$$

An example of occultation due to the morphology, condyle refolding, is illustrated in Fig. 4d where an axial slice of the object is delimited by $\overline{\text{Cylindrical}}(Z)$. Because a part was occulted during the first sagittal segmentation, the condyle refolding was not totally segmented. The addition of axial observers $o_r(x)$ and $o_l(x)$ in each condyle, right and left, solved the problem.

Figure 4e, f are sagittal views of the axial slices in Fig. 4a, b, respectively, illustrating the enhancement obtained by merging the Ray Casting surfaces of the
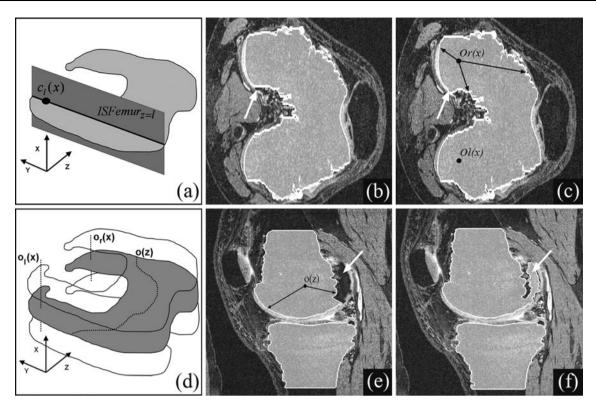
Fig. 4 **a** Illustration of the location of additional observers in the sagittal plane (*dark gray*) in the center of the condyle to process the additional segmentation in the axial plane (*light gray*). **b**, **c** Representative MRI axial slices of **b** incomplete segmented object delimited by $\overline{Cylindrical}(Z)$, and **c** completion by axial observers $o_r(x)$ and $o_l(x)$ and fusion. *White arrows* indicate the condyle refolding and the *black arrows* indicate the rays launched from observers. **d** Representation of the path followed by the sagittal observers, o(z), and axial observers, $ol(x)$ and $or(x)$. **e** Representation of MRI sagittal slices of incomplete segmented object delimited by $\overline{Cylindrical}(Z)$ and **f** combined result. In **e** and **f**, *white arrows* indicate the condyle refolding, *black arrows* indicate the rays launched from $o(z)$ (*black dot*)
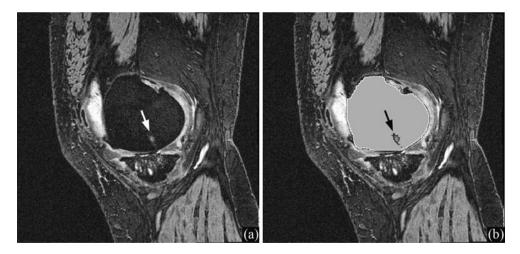

Fig. 5 **a** Representative MR images of sagittal underestimated segmentation due to the presence of a bone marrow lesion (*white arrow*). **b** The segmentation strategy allows proper segmentation eliminating the lesion (*black arrow*), final bone interior (*gray*) and frontier (*white line*)

segmented object. This merged segmentation succeeds in overcoming difficulties such as the presence of bone marrow lesions frequently observed in osteoarthritic bone (Fig. 5).

The developed fully automated segmentation processing time for a single patient is ∼25 min, including about 1 min for the initial approximation of bone location, 12 min for the initial sagittal segmentation and another
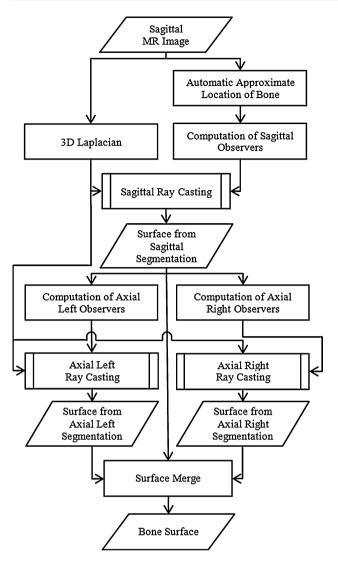
Fig. 6 Flow diagram of the general strategies for the fully automated knee bone segmentation in MR images

12 min for the two additional axial segmentations (see flow diagram, Fig. 6).

2.2 Cohort description and MRI acquisition

MR images of patients with knee osteoarthritis were obtained from a recently published study [29]. In brief, patients with primary symptomatic knee osteoarthritis of the medial tibiofemoral compartment were recruited from outpatient rheumatology clinics. Knee MR images from 161 osteoarthritis patients (aged 60 ± 8 years, Kellgren-Lawrence grade 2–3) corresponding to the according to protocol (ATP) population were used. The study was approved by the local ethics committees and all patients gave their oral and written informed consent to participate.

The MRI exams were carried out at five different sites and acquisitions were performed using 1.5 Tesla apparatus with integrated knee coil. The sequence consisted of optimized 3D-FISP acquisition with water excitation (Siemens, Erlangen, Germany) (Tr/Te = 22/9 ms, WaterExcitation, FoV = 160×160 mm, Matrix = 512×410, ST/SS = 1/0 mm, FlipAngle = 14°, Phase = AP) or 3D-SPGR acquisition with fat suppression (General Electric, Milwaukee, WI) (Tr/Te = 42/7 ms, FatSaturation, FoV = 160×160 mm, Matrix = 512×410, ST/SS = 1/0 mm, FlipAngle = 20°, Phase = AP). Rectangular FOV was adjusted to the various patient morphologies to optimize the acquisition time; the output image resolution was $0.3125 \times 0.3125 \times 1.0$ mm.

2.3 Validation

The developed fully automated bone segmentation was compared with validated semi-automated bone segmentation [18]. This semi-automated method was chosen because it is a validated method based on a completely different technique, 3D active contours, and which relies on ongoing quality control performed by the segmentation technician who initializes the reading. The inter-reader coefficient of this semi-automated segmentation was shown to be excellent ($r = 0.97$) for osteoarthritis patients [27]. The automatic segmentation was successfully performed on all the MR images of the study. The validation involves three types of comparison: the ASD, the average oriented surface distance, and the DSC.

In addition, the stability of the presented technology was evaluated using test–retest MR images, i.e., during the MR exam the patient was removed from and repositioned in the apparatus between the test and the retest acquisitions. MR images of four patients with knee osteoarthritis (seven test–retest images of left and right knees) were assessed in a blinded manner and were used to evaluate the reproducibility of the system using the ASD.

2.3.1 Bone surface

Comparison was first performed using the ASD [13] between each sample of both bone surfaces (a) obtained by the fully automated and the semi-automated methods for the same image or (b) obtained by the fully automated method for test–retest images of the same knee. This reflects either the different position of a contour *vis-à-vis* the same bone frontier in the image, or different options of segmentation. Since bone segmentation is a first step to articular marker assessment, an additional comparison was performed; the average oriented distance between bone surfaces within the cartilage domain with the semi-automatic bone segmentation [18].

2.3.2 Volume

Bone volume DSC was performed to compare the bones obtained by automatic and semi-automatic segmentation [18]. Commonly used in comparing techniques is the DSC [13] that is expressed for a single patient P as $\mathrm{DSC}(P) = 2|V_{\mathrm{semi}}(P) \cap V_{\mathrm{auto}}(P)|/(|V_{\mathrm{semi}}(P)| + |V_{\mathrm{auto}}(P)|)$, giving a mean result for a cohort of patients as $\overline{\mathrm{DSC}} = 1/|P| \sum_{P} \mathrm{DSC}(P)$.

The bone volume does not include all the bone in each image since neither semi-automatic nor automatic method could capture bone boundaries in the proximity of the upper and lower borders of the acquisition volume due to lack of contrast. Thus, the bone volume was artificially closed proximally for the femur and distally for the tibia, taking into account the presence of semi-automatic and automatic segmentation contours. Hence, for each patient P, the volume was defined as the 3D volume enclosed by the semi-automatic or automatic bone closed at the upper limit (femur) and lower limit (tibia) defined by the presence of semi-automatic and automatic contour.

3 Results

3.1 Bone surface

With regard to the distance between the semi-automatic and automatic bone surfaces, the ASD values were 0.50 ± 0.12 mm (median 0.48 mm [0.28–0.87]) for the femur and 0.37 ± 0.09 mm (median 0.35 mm [0.25–0.70]) for the tibia. When these values are compared to the acquisition resolution of 0.3125 mm, the ASD is 1.60 ± 0.38 pixels for the femur and 1.18 ± 0.29 pixels for the tibia. Of note, the ASD standard deviation is less than half a pixel.

For the test–retest evaluation, the measurements showed an excellent reproducibility with an average of less than half a pixel resolution and maximum value of less than a pixel for the femur, 0.19 ± 0.02 mm (median 0.18 mm [0.16, 0.22]) as well as for the tibia, 0.19 ± 0.03 mm (median 0.19 mm [0.14, 0.24]).

The evaluation of the average oriented distance between the semi-automatic and automatic bone surfaces within the cartilage domain gives values of 0.02 ± 0.07 mm (median 0.00 mm [−0.14, 0.29]) for the femur and -0.05 ± 0.10 mm (median −0.06 mm [−0.36, 0.33]) for the tibia. The average denotes the absence of systematic bias between both segmentations and the standard deviation indicates low changes in segmentation option.

3.2 Volume

The average bone volume DSC comparing semi-automatic and automatic methods showed excellent values: 0.94 ± 0.05 (median 0.96 [0.74–0.98]) was obtained for the femur and 0.92 ± 0.07 (median 0.95 [0.74–0.98]) for the tibia.

3.3 Localization of osteophytes and their volume evaluation

An osteophyte is an outgrowth of the bone close to the bone-cartilage interface and such structure is a characteristic of osteoarthritis. Although the volumetric measurement could be of major importance in the diagnosis of this disease and in clinical studies, to our knowledge, there is no report on a quantitative assessment of osteophytes in the human knee joint. Interestingly, our method, by taking the benefit of intermediate results further, permits osteophyte volume to be assessed.

For measurement of this structure, an osteophyte analysis domain was restricted to each bone metaphysis and epiphysis. For the femur, the osteophyte domain was defined on the femur bone surface by the largest object starting at the lower limit of the condyle and being equal to its convex shell. For the tibia, as there is no anatomic criterion that could be used, the domain was defined on the tibia bone surface by the object delimited by a plane 2 cm under the upper limit of the tibia epiphysis. In the respective domains, the geometric characteristic of the osteophytes can be localized by direct subtraction of the measured bone surface (see Sect. 2.1.6) from the filtered bone surface (see Sect. 2.1.5) limited to the osteophyte analysis domain in the cylindrical coordinate system. A selection of all the positive values corresponds to the areas of osteophytes. Once localized, the osteophyte volume can be evaluated in mm^3 and consists of the volume enclosed between the non-filtered and the filtered bone surface for both bones or for subregions.

4 Discussion

We reported the development and validation of a fully automated method for human knee bone (femur and tibia) segmentation on MR images taking into account the characteristics of the process which occurs in this tissue during osteoarthritis. Validation experiments comparing the developed fully automated method with a semi-automated segmentation method revealed excellent correlations.

The developed method is based on the Ray Casting technique which relies on the decomposition of the MR

images into multiple surface layers obtained by a Laplacian operator and on an approximation of the bone location obtained by intensity thresholding. This allows surface subset selection in the decomposed images which is then merged to obtain the whole segmented object (see flow diagram, Fig. 6). The Ray Casting technique was chosen to overcome problems encountered with MR images, thus producing a robust solution to the variable MR image quality. The Ray Casting technique historically used for 3D volume rendering [20] produces a geometric volume map (volume segmentation), and was recently used in object segmentation research for medical computer tomography (CT) imaging [22] as well as for radar imagery [12, 24]. Hence, the fully automated knee 3D MRI bone segmentation method presented in this study consists of the extraction of the information necessary to the Ray Casting followed by our implementation of the Ray Casting technique in which the surface selection process relies on prior knowledge of some bone interior points obtained automatically and autonomously using an approximation of the bone location. Moreover, the absence of prior shape model allows the use of the same technique for both the femur and tibia.

The main characteristic of the Ray Casting approach is its ability to process objects with discontinuous contour. However, caution should be exercised as it could cause leakage as seen with other non-model approaches [2, 14]. Moreover, although originally this technique only segmented star-shaped objects, this has been geometrically overcome by autonomously merging objects obtained from different initializations. Compared to other approaches, the simplicity and robustness provided by Ray Casting is a great advantage. First, the presented algorithm that works with only a few parameters automatically extracted from the signal can overcome problems encountered in a large scale imaging context, in which the image is often corrupted by noise, partial volume effect, or distortion. In addition, as this technique does not use a prior shape model, there was no need to model the influence of the disease on the shape geometry. This contrasts with other techniques that use average shape models [14, 23] or impose geometric priors [16] on the shape of the segmented objects, which do not allow the inclusion of disease characteristics. By being able to detect bone irregularities, the developed method can allow the detection, and quantitative evaluation of osteophytes. Quantitative osteophyte measurement is of importance, as the methods described in the current literature are performed only on radiograph images and are semi-quantitative. Such methods are not sensitive, are dependent on the acquisition angle of the knee, and evaluate only the osteophytes at the periphery of the bone and only at the sides of the condyle and tibia. The automated method, as

described here, is quantitative and evaluates all the osteophytes, i.e., peripheral and central (under the cartilage). Another bone alteration is the bone marrow lesion; however, in this study, evaluation of these latter structures was not performed as the sequence used was a T1* gradient echo sequence known to underestimate their volume [31].

A limitation of the controlled filter method design could be that although extreme precautions were taken to enable the correction of inner bone signal while preserving the initial measurement, some exceptional configuration could occur, e.g., significant Fat Sat failures, truncation artifacts and strong flow artifacts, which should, at a certain point, cause the rejection of the MR images. Similarly, thin edemas widely spread near the bone interface could prevent the filter from recovering the integrality of the bone interface.

Validation experiments comparing the newly developed fully automated method with the semi-automated method revealed a very low deviation, less than half a pixel size, when the ASD between the two bone surfaces was measured. However, the bone surface ASD obtained was better than that of Fripp et al. [8] using additional information, where a higher ASD value (0.73 mm) was obtained, but contrasts with another Fripp et al. [9] reported data, using a different methodology from the previous [8], a model approach having a value of 0.16 mm on the bone-cartilage interface. Of note, the Fripp et al. works were performed on healthy individuals, and as is well-known, in osteoarthritis patients the bone-cartilage interface delineation is more difficult to achieve due to presence of osteophytes, of bone lesions in the subchondral bone and in the bone marrow, in addition to the lower image quality (mainly lower contrast and lower quality of the edges) caused by excessive synovial fluid. On the other hand, comparable DSC values were found in the two Fripp et al. works [8, 9], where values of 0.93 ± 0.03 and 0.92 ± 0.03 and 0.95 ± 0.06 and 0.95 ± 0.07 [8, 9] were found, respectively, for the femur and tibia.

All together, the validation analyses performed on a large osteoarthritis cohort revealed excellent results in terms of stability and accuracy, highlighted by the low standard deviation of the ASD, high volume correlation coefficient and DSC. The slightly better results obtained for the tibia compared to the femur may be explained by the simpler geometry of its articular domain producing less partial volume effects. Additional analyses looking at the difference between the brand of MR apparatus used (Siemens vs. GE) and the presence of bone marrow lesions revealed no difference in ASD or DSC and no statistical trend for ASD between the number of subregions in which a bone marrow lesion was present (0–4 in the femur; 0–2 in the tibia) (data not shown).
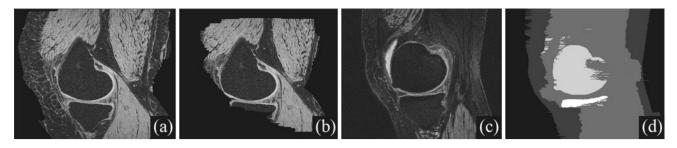
Fig. 7 **a**, **b** A sagittal slice of the image restricted to the $Leg_{z=t}$ set (**a**) and restricted to the smaller $MCart_{z=t}$ set (**b**). The *black* parts of the slices denote the outside of each set while parts with image content denote the inside of each set. **c** A representative sagittal slice and **d** the sets $Leg_{z=t}$, $MCart_{z=t}$, *IFemurandITibia*, respectively, in *dark*, *medium*, *light* and *bright gray*

As one of the main objectives for automatic bone segmentation is to study the articular domain, the accuracy of the automatic segmentation evaluated by the average oriented distance between bone surfaces within the cartilage domain provides a high level of confidence for knee articular marker assessments.

A primary advantage of this newly developed automated bone segmentation method is the possibility of intensive and autonomous computation, enabling images from a large cohort of patients to be analyzed in a shorter time and, more importantly, increased stability of the reading. Indeed, this method will prevent major problems encountered with the semi-automated segmentation method, including contrast, intensity, and gamma tuning for the image display, which have an important influence on the final segmentation contours. From a clinical/physician point of view the low ASD and high DSC of the presented fully automatic method assure the accuracy of results.

Appendix: Bone Localization Procedure

The Ray Casting technique requires some prior knowledge including an approximation of the bone location to set the observers in each image. This appendix describes the autonomous procedure.

The analysis of the intensity histogram H shows a mixture of two probability densities, one centered in the low values, and the other in the high values. Because of its stability and robustness, the Otsu's algorithm [25] was chosen to analyze the histogram, giving a decomposition of the histogram as a sum of two Gaussian distributions $N(\mu_d, \sigma_d)$ and $N(\mu_b, \sigma_b)$. The histogram's dark tissue peak is μ_d and bright tissue peak is μ_b. Values inferior to the dark peak are called very dark and values superior to the bright peak, very bright. Otsu's algorithm also provides a decision threshold s of separation between dark and bright, and mixture parameters α_d and α_b, allowing the histogram to be written:

$$H(I) \cong \alpha_d N(\mu_d, \sigma_d) + \alpha_b N(\mu_b, \sigma_b) \ with \ \alpha_d + \alpha_b = 1 \quad (6)$$

An algorithm was designed to capture *IFemur* and *ITibia* on the MR image where the bones, femur and tibia (dark), are surrounded by cartilage and muscle (very bright), further surrounded by fat (dark), then skin (bright), and finally the background (very dark).

One has to start from Ω and evaluate the following set in order of decreasing size, where *Leg* is the leg, and *MCart* is the cartilage and muscle set:

$$\Omega \supset Leg \supset MCart \supset \{IFemur \cup ITibia\} \quad (7)$$

Let us define $H_{convex}(X)$ the convex hull of a finite set X. Considering the decision threshold s, the anatomical convexity of the leg in each axial slice, and the brightness of the tissues, each axial subset of the leg can be approximated by

$$Leg_{x=h} \equiv H_{convex}\{(y,z) \quad I_{x=h}(y,z) \geq s\} \quad (8)$$

In order to have an appropriate cartilage and muscle set, surrounding femur and tibia, the selection relies on bright intensity and on convexity properties. Thus, *MCart* can be written as:

$$MCart_{x=h} \equiv H_{convex}\{(y,z) \in Leg_{x=h}, \quad I_{x=h}(y,z) \geq \mu_b\} \quad (9)$$

Figure 7a, b shows two sagittal slices of the intermediate results, the $Leg_{z=t}$ set (Fig. 7a) and the $MCart_{z=t}$ set (Fig. 7b).

Finally, the bone part inside this set can be identified by the very dark tissue inside *MCart* such that:

$$IFemurTibia_{x=h} \equiv ((y,z) \in MCart_{x=h}, \quad I_{x=h}(y,z) \leq \mu_d) \quad (10)$$

Femur and tibia sets are easily defined by separating the two largest components of *FemurTibia* as shown in Fig. 7c

and d, where the largest is the set *Femur* and the second largest is the set *Tibia*. To facilitate the decomposition, an opening morphology operator ∘ is used [12] with structuring disk *D* of small diameter, e.g. five pixels. The set *FemurTibia* admits the following decomposition:

$$IFemurTibia \circ D = IFemur \cup ITibia$$
$$\cup \cdots Other\ small\ objects \qquad (11)$$

References

1. Berthiaume MJ, Raynauld JP, Martel-Pelletier J, Labonté F, Beaudoin G, Bloch DA, Choquette D, Haraoui B, Altman RD, Hochberg M, Meyer JM, Cline GA, Pelletier JP (2005) Meniscal tear and extrusion are strongly associated with the progression of knee osteoarthritis as assessed by quantitative magnetic resonance imaging. Ann Rheum Dis 64:556–563
2. Dalvi R, Abugharbieh R, Wilson DC, Wilson D (2007) Multi-contrast MR for enhanced bone imaging and segmentation. Conf Proc IEEE Eng Med Biol Soc 2007:5620–5623
3. Ding C, Cicuttini F, Jones G (2007) Tibial subchondral bone size and knee cartilage defects: relevance to knee osteoarthritis. Osteoarthr Cartil 15:479–486
4. Dogdas B, Shattuck D, Leahy RM (2002) Segmentation of the skull in 3D human MR images using mathematical morphology. Proceedings of the SPIE. Med Imaging 4684:1553–1562
5. Felson DT, Niu J, Guermazi A, Roemer F, Aliabadi P, Clancy M, Torner J, Lewis CE, Nevitt MC (2007) Correlation of the development of knee pain with enlarging bone marrow lesions on magnetic resonance imaging. Arthritis Rheum 56:2986–2992
6. Folkesson J, Dam E, Olsen OF, Pettersen P, Christiansen C (2005) Automatic segmentation of the articular cartilage in knee MRI using a hierarchical multi-class classification scheme. Med Image Comput Comput Assist Interv 8:327–334
7. Folkesson J, Olsen OF, Pettersen P, Dam E, Christiansen C (2005) Combining binary classifiers for automatic cartilage segmentation in knee MRI. In: Liu Y, Jiang T, Zhang C (eds) Lecture notes in computer science. Springer-Verlag, Berlin, pp 230–239
8. Fripp J, Bourgeat P, Crozier S, Ourselin S (2007) Segmentation of the bones in MRI of the knee using phase, magnitude and shape information. Acad Radiol 10:1201–1208
9. Fripp J, Crozier S, Warfield SK, Ourselin S (2007) Automatic segmentation of the bone and extraction of the bone-cartilage interface from magnetic resonance images of the knee. Phys Med Biol 52:1617–1631
10. Fripp J, Warfield SK, Crozier S and Ourselin S. (2007) Automatic segmentation of articular cartilage in magnetic resonance images of the knee. Lecture notes in computer science, medical image computing and computer-assisted intervention 10:186–194
11. Fripp J, Crozier S, Warfield SK, Ourselin S (2010) Automatic segmentation and quantitative analysis of the articular cartilages from magnetic resonance images of the knee. IEEE Trans Med Imaging 29:55–64
12. Gambini J, Mejail M, Jacobo J and Delrieux C. (2004) SAR image segmentation through B-spline deformable contours and fractal dimension. Proceedings of the international society for photogrammetry and remote sensing (ISPRS) July 15–23, Istanbul, Turkey
13. Gerig G, Jomier M and Chakos M. (2001) VALMET: A new validation tool for assessing and improving 3D object segmentation. Proceedings of the international society and conference series on medical image computing and computer-assisted intervention 2208:516–523
14. Grau V, Mewes AUJ, Alcaniz M, Kikinis R, Warfield SK (2004) Improved watershed transform for medical image segmentation using prior information. IEEE Trans Med Imaging 23:447–457
15. Hamarneh G, Li X (2009) Watershed segmentation using prior shape and appearance knowledge. Image Vis Comput 27:59–68
16. Heinze P, Meister D, Kober R, Raczkowsky J, Worn H (2002) Atlas-based segmentation of pathological knee joints. Stud Health Technol Inform 85:198–203
17. Kapur T, Beardsley PA, Gibson SF, Grimson WEL and Wells WM. (1998) Model based segmentation of clinical knee MRI. Proceedings of the IEEE international workshop on model-based 3D image analysis, Bombay, India:97–106
18. Kauffmann C, Gravel P, Godbout B, Gravel A, Beaudoin G, Raynauld J-P, Martel-Pelletier J, Pelletier J-P, DeGuise JA (2003) Computer-aided method for quantification of cartilage thickness and volume changes using MRI: validation study using a synthetic model. IEEE Trans Biomed Eng 50:978–988
19. Kubassova O, Boyle RD and Pyatnizkiy M. (2005) Bone segmentation in metacarpophalangeal MR data. Proceedings of the third international conference on advances in pattern recognition (ICAPR):726–735
20. Levoy M (1990) Efficient ray tracing of volume data. ACM Trans Gr 9:245–261
21. Loeuille D, Chary-Valckenaere I, Champigneulle J, Rat AC, Toussaint F, Pinzano-Watrin A, Goebel JC, Mainard D, Blum A, Pourel J, Netter P, Gillet P (2005) Macroscopic and microscopic features of synovial membrane inflammation in the osteoarthritic knee: correlating magnetic resonance imaging findings with disease severity. Arthritis Rheum 52:3492–3501
22. Lorenz C, von Berg J (2005) Fast automated object detection by recursive casting of search rays. Int Congr Ser 1281:230–235
23. Lorigo LM, Faugeras O, Grimson WEL, Keriven R and Kikinis R. (1998) Segmentation of bone in clinical knee MRI using texture-based geodesic active contours. Lecture notes in computer science, proceedings of the first international conference on medical image computing and computer-assisted intervention 1496:1195–1204
24. Mayunga SD, Coleman DJ, Zhang Y (2007) A semi-automated approach for extracting buildings from QuickBird imagery applied to informal settlement mapping. Int J Remote Sens 28:2343–2357
25. Otsu N (1979) A threshold selection method from gray-level histograms. IEEE Trans Syst Man Cybern 9:62–66
26. Pelletier JP, Raynauld JP, Abram F, Haraoui B, Choquette D, Martel-Pelletier J (2008) A new non-invasive method to assess synovitis severity in relation to symptoms and cartilage volume loss in knee osteoarthritis patients using MRI. Osteoarthr Cartil 16(Suppl 3):S8–S13
27. Raynauld JP, Kauffmann C, Beaudoin G, Berthiaume MJ, de Guise JA, Bloch DA, Camacho F, Godbout B, Altman RD, Hochberg M, Meyer JM, Cline G, Pelletier JP, Martel-Pelletier J (2003) Reliability of a quantification imaging system using magnetic resonance images to measure cartilage thickness and volume in human normal and osteoarthritic knees. Osteoarthr Cartil 11:351–360
28. Raynauld JP, Martel-Pelletier J, Berthiaume MJ, Labonté F, Beaudoin G, de Guise JA, Bloch DA, Choquette D, Haraoui B, Altman RD, Hochberg M, Meyer JM, Cline G, Pelletier JP (2004) Quantitative magnetic resonance imaging evaluation of knee osteoarthritis progression over two years and correlation with clinical symptoms and radiologic changes. Arthritis Rheum 50:476–487

29. Raynauld JP, Martel-Pelletier J, Bias P, Laufer S, Haraoui B, Choquette D, Beaulieu AD, Abram F, Dorais M, Vignon E, Pelletier JP (2009) Protective effects of licofelone, a 5-lipoxy-genase and cyclo-oxygenase inhibitor, versus naproxen on carti-lage loss in knee osteoarthritis: a first multicentre clinical trial using quantitative MRI. Ann Rheum Dis 68:938–947

30. Roemer FW, Frobell R, Hunter DJ, Crema MD, Fischer W, Bohndorf K, Guermazi A (2009) MRI-detected subchondral bone marrow signal alterations of the knee joint: terminology, imaging appearance, relevance and radiological differential diagnosis. Osteoarthr Cartil 17:1115–1131

31. Wolf M, Welerich P, Niemann H (1997) Automatic segmentation and 3D-registration of a femoral bone in MR images of the knee. Pattern Recognit Image Anal 7:152–165

32. Yuille AL, Poggio TA (1986) Scaling theorems for zero cross-ings. IEEE Trans Pattern Anal Mach Intell 8:15–25